# Dichotomous Array of Chiral Quantum Corrals by a Self-Assembled Nanoporous Kagome Network

**ARTICLE** *in* NANO LETTERS · JULY 2009

Impact Factor: 13.59 · DOI: 10.1021/nl901700b · Source: PubMed

NANO LETTERS

XXXX
Vol. xx, No. x
-

# Dichotomous Array of Chiral Quantum Corrals by a Self-Assembled Nanoporous Kagomé Network

**Florian Klappenberger,*,† Dirk Kühne,† Wolfgang Krenner,† Iñaki Silanes,‡,§ Andres Arnau,‡,|| F. Javier García de Abajo,⊥,¶ Svetlana Klyatskaya,# Mario Ruben,# and Johannes V. Barth†**

*Physik Department E20, TU München, Germany, Donostia International Physics Center (DIPC) and Departamento de Fisica de Materiales and Unidad de Fisica de Materiales, E-20018 San Sebastian, Spain, Instituto de Óptica—CSIC, Serrano 121, 28006 Madrid, Spain, and Karlsruhe Institute of Technology (KIT), Forschungszentrum Karlsruhe, Karlsruhe, Germany*

*Received May 29, 2009*

## ABSTRACT

**The confinement of surface-state electrons by a complex supramolecular network is studied using low-temperature scanning tunneling microscopy and rationalized by electronic structure calculations using a boundary element method. We focus on the self-assembly of dicarbonitrile-sexiphenyl molecules on Ag(111) creating an open kagomé topology tessellating the surface into pores with different size and symmetry. This superlattice imposes a distinct surface electronic structure modulation, as observed by tunneling spectroscopy and thus acts as a dichotomous array of quantum corrals. The inhomogenous lateral electronic density distribution in the chiral cavities is reproduced by an effective pseudopotential model. Our results demonstrate the engineering of ensembles of elaborate quantum resonance states by molecular self-assembly at surfaces.**

The manipulation of individual atoms by scanning tunneling microscopy (STM) made it possible to build nanoscale structures for electron confinement, the so-called quantum corrals.[1] The corresponding scanning tunneling spectroscopy (STS) measurements allowed visualizing the resulting resonance states of the originally nearly free two-dimensional electron gas supplied by the surface-state electrons of the employed Cu(111) surface. This work inspired several impressive demonstrations of exquisite control over electronic quantum states,[2,3] including the quantum mirage effect projecting the Kondo signature of a magnetic adatom to a remote location.[4] More recently, the coherent scattering present in such structures was employed for quantum holographic encoding.[5] Sophisticated theories for the interpretation of these experiments have been developed,[6−8] and based thereupon, systematic quantum corral wave function engineering was proposed.[9]

An alternate route to design architectures for the surface state quantum laboratory is provided by self-assembly of adsorbate superlattices.[10−13] This approach provides inherent advantages regarding ease of fabrication and parallel processing and could be furthermore expanded to steer the arrangement of individual atoms in quantum resonators.[14,15] However, to date mainly rather simple confinement geometries, such as one-dimensional trenches have been investigated. Here we explore the supramolecular engineering of complex quantum corrals. We employ surface-confined supramolecular self-assembly[16] to achieve an intricate tessellation of the Ag(111) surface.[17] Our STS observations reveal how the presence of the deployed nanoporous chiral kagomé network with regular cavities induces confinement of the quasi-two-dimensional surface-state electron gas creating an ensemble of quantum corrals. We have reproduced the characteristics of the pertaining spectral electron eigenstate densities by electronic structure calculations using a boundary element method.

In our vacuum apparatus (base pressure $\sim 3 \times 10^{-11}$) a clean Ag(111) surface was prepared by repeated cycles of $Ar^+$ sputtering and annealing to 470 °C. Dicarbonitrile-sexiphenyl ($NC-Ph_6-CN$) molecules were synthesized as described in ref 18 and sublimated from a quartz glass

* Corresponding author, florian.klappenberger@ph.tum.de.
† Physik Department E20, TU München.
‡ Donostia International Physics Center (DIPC) and Departamento de Fisica de Materiales and Unidad de Fisica de Materiales.
§ Instituto de Física de Cantabria (IFCA).
|| Departamento de Fisica de Materiales UPV/EHU, Facultad de Quimica and Centro de Fisica de Materiales del Centro Mixto CSIC-UPV/EHU.
⊥,¶ Instituto de Óptica—CSIC.
# Karlsruhe Institute of Technology (KIT), Forschungszentrum Karlsruhe.

10.1021/nl901700b CCC: $40.75 

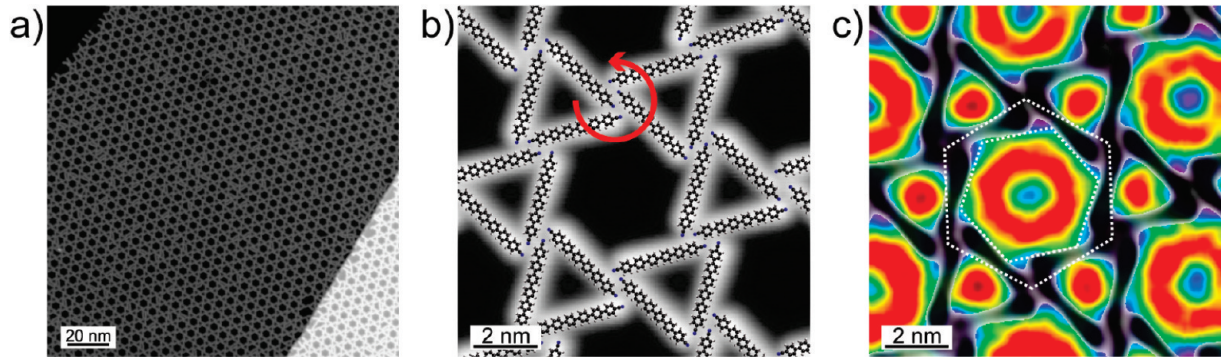


**Figure 1.** (a) Topograph of large-area domains of a porous, chiral kagomé network self-assembled by evaporating ~0.4 ML of NC−$Ph_6$−CN onto the Ag(111) surface. (Tunneling current $I_T = 0.14$ nA, bias voltage $V_B = 1.25$ V.) (b) High-resolution image of the kagomé structure with superimposed ball-and-stick models of the molecules. ($I_T = 0.1$ nA, $V_B = -0.5$ V.) The network divides the surface into a regular arrangement of two different types of pores (hexagons and triangles). Chirality originates form the counterclockwise rotating nodes. (c) Constant-current d*I*/d*V* map (rainbow color coded) simultaneously taken while scanning the topography (displayed in black, $V_B = 320$ mV). The local density of states is periodically modulated by the presence of the organic network. The dichotomous confinement with quasi-hexagonal and triangular-terminated areas imposes a distinct electronic structure in each type of pore. The two white dotted hexagons highlight the rotation of the electronic mode inside the quasi-hexagon with respect to the kagomé lattice caused by the chirality of the network.

crucible inside a Knudsen cell held at 572 K onto the Ag substrate at room temperature (RT). For the organic layers, a deposition time of 10 min resulted in a molecular coverage of approximately 0.4 monolayers (ML), with one monolayer defined as a saturated layer of dense-packed molecules. The samples were transferred into a homemade[19] beetle-type low-temperature STM, in which data were recorded at 7 K. STS was accomplished in an open-feedback loop operation mode with set points as given in the corresponding figure captions and modulation frequencies between 1600 and 1800 Hz with an amplitude of 5 mV rms. The lock-in time constant was 100 ms. The d*I*/d*V* maps of Figure 4 were extracted from a set (84 × 84) of such point spectra, with a reduced number of bias points that were equally distributed over the area of the topographic image. All spectra were normalized so that the differential conductance averaged over the energy range between −180 and −130 mV equals unity. The constant-current d*I*/d*V* map of Figure 1 was simultaneously measured while recording the corresponding topograph with both the feedback loop time constant and the scan time per pixel much longer than the period of the bias modulation.

An earlier study[17] on dicarbonitrile-polyphenyl molecules (NC−$Ph_x$−CN) demonstrated that this class of ditopic organic molecules assemble in networks with different symmetry and complexity depending on the length of the polyphenyl backbone. For the case of $x = 5$, a complex, chiral kagomé network formed domains with lateral dimensions reaching the micrometer range. Here, we evaporated approximately 0.4 ML of NC−$Ph_6$−CN onto the Ag(111) surface and found a similar chiral kagomé topology (Figure 1a), presenting larger pores due to the increased number of phenyl moieties. This supramolecular arrangement again features a micrometer domain size with a low defect density. Some of the pores contain additional molecules as guests. A high-resolution image (Figure 1b) highlights that the kagomé structure divides the surface into two types of nanopores. Six molecules (white protrusions) form a larger, quasi-hexagonal-shaped pore, which is surrounded by six triangular-shaped cavities, each of them formed by three molecules. Chirality originates from the supramolecular organization of the achiral molecules mediated by weak lateral interaction. As can be seen from the superimposed ball-and-stick models of the molecules, the end groups of four molecules come together at each node. Hereby, they are not pointing to the node center but are laterally offset, forming a chiral rotor motif (red arrow) turning counterclockwise. A constant-current d*I*/d*V* map (Figure 1c, rainbow color coded, bias voltage $V_b = 0.32$ V) demonstrates the pertaining periodic pattern of the local differential conductance which is, within the Tersoff−Harmann approximation,[20] directly proportional to the local density of states (LDOS).[21] Thus, the self-assembled organic network imposes a novel, complex electronic structure to the underlying metal substrate, not only locally but over macroscopic extent. The superimposed, inverted topograph of the same measurement (molecules in black) highlights the different electronic structure in the two different types of cavities, i.e., the dichotomous confinement character. The chirality of the network is reflected in the chirality of the imposed electronic structure. The outline of the green area of the mode inside the quasi-hexagonal-shaped pore (inner white dotted line in Figure 1c) defines a hexagon rotated clockwise against the hexagon made up by the centers of the surrounding nodes (outer white dotted line).

To quantify the novel electronic structure of the substrate, we have performed spectroscopic measurements at the points indicated in Figure 2a. The reference spectrum (Figure 2b, gray curve) taken on the clean substrate shows the steplike onset and the nearly constant LDOS connected with the surface band starting at an offset energy near to −65 meV.[22,23] The spectra acquired over the supramolecular assembly exhibit prominent position-dependent modulations of the differential conductance. At the center of the large pore (black curve), two dominant peaks occur at bias voltages $V_B = -20$ mV and $V_B = 280$ mV. Halfway between the center and the border of the quasi-hexagon (red curve), a

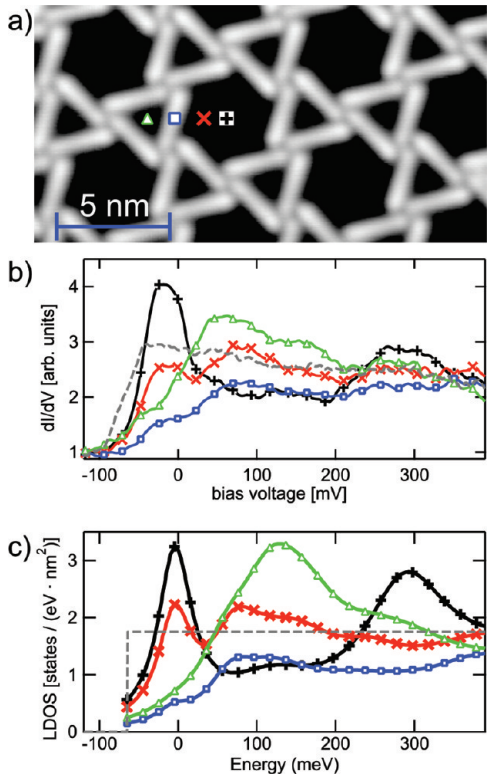


**Figure 2.** (a) Topograph of the purely organic kagomé network. The symbols depict the positions at which the d*I*/d*V* spectra of (b) were taken. (b) Experimental d*I*/d*V* spectra demonstrating a strong position-dependent modulation of the LDOS. The nearly constant LDOS of the pristine surface (gray dashed line) is shown for comparison. (c) Theoretical spectra simulated with the boundary element method at the same positions as in (b) (see symbols in (a)).

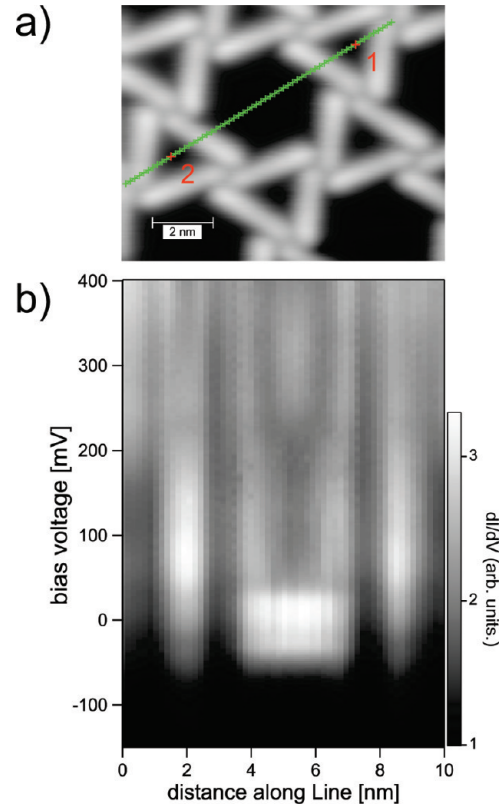


**Figure 3.** (a) STM topograph showing the line along which the d*I*/d*V* spectra of (b) were taken. (b) Plot of the differential conductance in the −120 to 400 mV bias range. A linear grayscale is used for the spectral intensity.

third resonance appears at $V_B = 80$ mV in between the two previous ones. The spectrum taken above the backbone of a molecule (blue curve) exhibits the strongest reduction of the surface state LDOS. In the center of the smaller, triangular pore the lowest-lying peak appears at $V_B = 60$ mV bias voltage, thus at a remarkably higher energy than that of the first resonance in the larger pore. We attribute the LDOS modulation to quantum mechanical confinement of the surface-state band by the nanoporous network. This interpretation is strongly supported by the good agreement between experimental (Figure 2b) and simulated spectra (Figure 2c), which will be discussed in detail later on.

To better understand the spectral distribution of the different resonant states, a series of d*I*/d*V* spectra (Figure 3b) was taken along a line connecting two nodes of opposing triangles (Figure 3a). The measurement presented in Figure 3 was conducted on a domain featuring the opposite chirality (clockwise rotating nodes) than the one displayed in Figure 1b. Several of these line spectra have been obtained on both enantiomers of the kagomé structure resulting in consistent spectral distributions. In the central, quasi-hexagonal pore, the first resonance displaying one maximum (no node) at the center of the hexagon is visible around $V_B = -10$ mV. With increasing energy the resonance is displaced by a distinct two-peak structure between $V_B = 50$ mV and $V_B = 200$ mV. For even higher energies a state with three antinodes appears ($V_B \sim 250$ mV). In the triangular pores the first resonance is centered around $V_B = 75$ mV and extends over an energy range ($-50$ mV $< V_B <$ 200 mV) roughly 2.5 times wider than the first resonance in the larger pore. The spectra in the vicinity of points 1 and 2 reveal slightly different behavior that reflects the asymmetry of the triangles with respect to the scan-line center (end-triangles pointing up and down). In pore 2, the single maximum resonance turns into two maxima at voltages exceeding 300 mV. In contrast, in pore 1 no second maximum can be observed. The whole set of spectra clearly indicates that the kagomé network divides the surface into a regular array of two types of pores with different electronic structure. The distinct resonances appear with a varying spatial distribution and energy width reflecting the effects of both elastic and inelastic scattering due to coupling of surface-state electrons with projected bulk bands and electron−electron interactions, respectively.

Next, to fully characterize the spatial extent of the different resonances and the pertaining electron density distribution, we constructed differential conductance maps (Figure 4) at bias voltages corresponding to the different peaks in the point spectra. At $V_B = 0$ mV, a bright domelike structure dominates in the center of the hexagonal pore, while underneath the molecules the electronic density is strongly reduced (cf. parts a and b of Figure 4). Upon increase of $V_B$ to 125 mV, the intensity distribution in the quasi-hexagon exhibits a minimum in the center, whereas the triangular pores exhibit even brighter intensity than the large pores (Figure 4c). For both

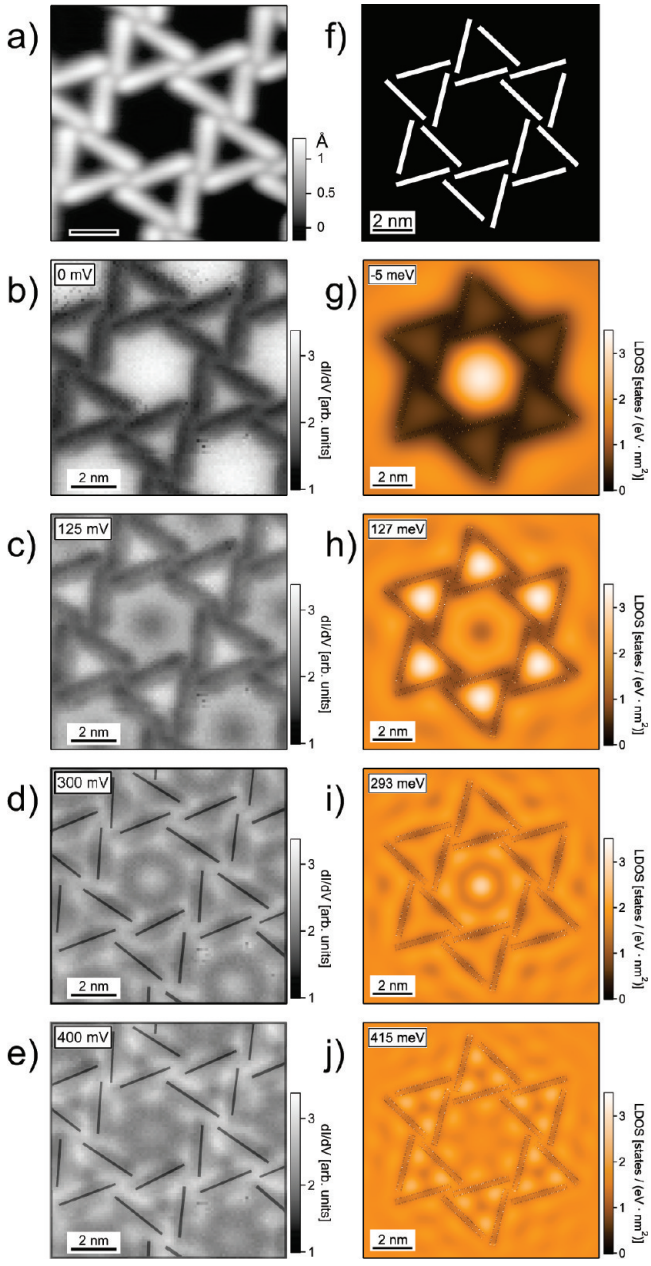


**Figure 4.** The kagomé network (topograph in (a)) induces standing wave patterns (b−e) in the otherwise uniform measured LDOS. (f) The model structure used for the BEM calculations. Black and white areas correspond to $V = 0$ and $V = 500$ meV, respectively. At all bias voltages, there is excellent agreement between experimental maps (b−e), which were retrieved from open-feedback loop point spectra, and calculated LDOS distributions (g−j).

bias voltage (cf. parts b and c of Figure 4), the envelope of the quasi-hexagon mode reflects the chirality of the network by its ratched wheel border, i.e., nearly hexagonal, but with an asymmetric dent at each corner. At higher energies ($V_B$ = 300 mV, Figure 4d) a sombrero-shaped pattern is visible; i.e., a central maximum is surrounded by a circular depression, which is in turn surrounded by a ring of bright intensity near the hexagon borders. The ring is modulated such that the strongest intensity is near the asymmetric corners. Furthermore, a three-winged propeller-shape distribution of the LDOS is visible in the triangular pores. Each propeller evolves into a set of three bright lobes at the highest bias values ($V_B$ = 400 mV, Figure 4e), whereby inside the hexagonal pores the central maximum has almost disappeared with the modulation of the outer ring persisting. The maps taken at high bias values emphasize how the chiral arrangement of the molecules introduces chiral electronic properties to the underlying Ag surface.

We have gained further insight into the electron confinement properties of the network through model simulations using a scalar version of the electromagnetic boundary element method (BEM) described in ref 24. In our BEM, the Schrödinger equation is solved for a planar patterned surface, which is modeled through homogeneous regions of constant potential describing the kagomé motif. The boundaries between these regions are considered to be abrupt, and the solution for the wave function is expressed in terms of auxiliary electron boundary sources, which are propagated throughout each homogeneous region via the electron Green's function of the corresponding infinite, homogeneous surface. This involves integration of the sources over the boundary contours. The auxiliary sources are then determined from the continuity of both the wave function and its gradient, thus setting up a system of integral equations that we solve upon discretization using standard numerical linear-algebra techniques. A total of 1296 boundary discretization points have been required to achieve convergence in our model structure. Here, we obtain the LDOS at a given spatial location from the imaginary part of the reflected wave function produced by an electron point source placed at that location.

We have defined the effective scattering potential landscape as depicted in Figure 4f, in which the molecules are described by rectangles (white) with the length (2.9 nm) and the width (0.25 nm, carbon−carbon distance perpendicular to the long molecular axis) given by the molecules and with an effective scattering potential value of $V_{mol}$ = 500 meV with respect to the remaining area (black). For the surface-state electron band, we have assumed an effective electron mass $m^* = 0.42m_e$, where $m_e$ is the free electron mass, consistent with the measured band of the unpatterned Ag(111) surface, an onset energy of −65 meV,[22,25] and an energy-independent broadening (25 meV) of all electronic states. The latter represents a single phenomenological value taking into account both of the two above-mentioned elastic and inelastic contributions to the energy width of the surface-state resonances.

Using the BEM, we have calculated the energy-dependent LDOS(E) at different positions and compared it to the measured d$I$/d$V$ spectra. Despite the simplicity of the model and the fact that only one fitting parameter, namely, $V_{mol}$, has been used, the simulated spectra (Figure 2c) agree very well with the measured point spectra (Figure 2b) regarding both peak positions and peak intensities. More precisely, two clear maxima (−5 and 293 meV) are present in the center of the quasi-hexagon (black, plus symbols) and an intermediate peak shows up at 81 meV at a halfway position (red, crosses). In the smaller triangular pore (green, triangles), the lowest-lying resonance is upshifted to 127 meV. Right on top of a molecule (blue, squares), the first maximum appears

at a similar energy as in the triangular pore, but with a reduced height.

In general, the measured spectroscopic features have similar broadening as the simulated ones. We attribute the sources of lifetime broadening to both inelastic (electron−electron, electron−phonon) and elastic (coupling to projected bulk bands at the same energy) scattering, as well as to the finite transmission through the potential barriers. The two peaks of the experimental spectrum taken in the center of the quasi-hexagon have widths of 56 and 153 mV at the differential conductance value of the reference curve. The time taken by surface-state electrons of the corresponding *k*-vectors to travel the distance between two parallel molecules of a hexagon boundary is ∼15 and ∼6 fs. The broadening connected with such times amounts to 45 and 105 meV, respectively, indicating that interaction takes place mainly at the boundaries. We suggest, that inelastic and elastic broadening dominate for the electron energy $E \ll V_{mol}$, while finite transmission constitutes the more the nearer $E$ gets to $V_{mol}$. In the theoretical curves, inelastic scattering processes are included only phenomenologically via a Lorentzian width (25 meV) of the electron states in the BEM simulation. The widths of the peaks in the calculated spectra of the center of the quasi-hexagon pore (55 and 160 meV, taken at the state density of the reference curve, cf. Figure 2c) outrange the Lorentzian width by far and are in good agreement with the experimental values. This demonstrates that the sole effect of the scattering barriers already leads to spectral features of finite width and supports our description of the barrier potential.

Conductance maps (LDOS($x$,$y$)) were calculated at the relevant energies where the maxima in the point spectra indicate the existence of a resonance. To facilitate quantitative comparison between different maps, all simulations are displayed using an identical color scale in Figure 4. The same is true for the experimental maps. An inspection of the measured maps demonstrates that the simulated standing-wave patterns reproduce the experimental data in great detail. A central bright dome-shaped resonance, surrounded by triangles of much weaker intensity for the lowest energy map (Figure 4g), is clearly discernible against the bright intensity in the triangles, combined with a ratchet-wheel wave pattern of weaker intensity for the second map (Figure 4h). For the next higher energy (293 meV, Figure 4i), the sombrero pattern with the modulated outer rim in the quasi-hexagon and the propeller pattern inside the triangles resemble closely the experiment. With an increase in the wave vector of the surface-state electrons, their de Broglie wavelength becomes shorter. Accordingly, in the 415 meV map (Figure 4j) the features exhibit the shortest lateral dimensions of the whole series, namely, three small protrusions in each triangle surrounding a central depression. In the larger pore the central protrusion appears with reduced brightness compared to Figure 4i. Both of these features are similarly reflected in the measured data.

The remarkable agreement between theory and experiment is clear indication that the physically relevant properties regarding confinement and scattering are well described by our simple model of rectangular areas featuring a constant effective potential. In additional calculated maps, we tested the influence on the LDOS due to interaction between neighboring pores by defining triangles having one, two, or three neighboring triangles. We found that only minor differences are visible in the conduction maps. We conclude, that transmission through the cavity boundaries is weak and interaction between cavities is therefore small and does not play a major role in the formation of the standing wave patterns. Accordingly, in a simple one-dimensional quantum mechanical calculation of the reflection of an electron wave under perpendicular incidence scattered by a barrier with the thickness and potential height as used in the BEM simulation, we obtained a reflectivity $\rho_{Kag} = 0.7$ at $E_F$. This compares to reflectivity values of $\rho_{desc} = 0.85$ and $\rho_{asc} = 0.5$ for a descending and an ascending step on the pristine Ag(111) surface, respectively.[25] It has already been shown[12] that rows of organic methionine molecules on Ag(111) can lead to reflection ($\rho_{meth} = 0.85$) of similar strength as in the descending step case. Gross et al. have studied the scattering of Cu(111) surface-state electrons by so-called Lander molecules, which contain an extended aromatic backbone and di-*tert*-butylphenyl spacers.[26] They demonstrated that the aromatic backbone dominates the scattering properties of the molecules, although only the butyl spacers were in direct contact with the substrate. Their assumption that the $\pi$ system is responsible for the interaction with the surface-state electrons is confirmed by our study. In a semiempirical calculation within the PM1 framework[27] of NC−$Ph_6$−CN in the gas phase, the frontier orbitals HOMO-2 to LUMO+2 feature $\pi$-orbitals conjugated over the entire molecule, including sexiphenyl backbone and carbonitrile groups. The geometry of these orbitals tentatively explains why our simple rectangular model for the scattering properties of the molecules works so well. A monolayer of sexiphenyl on Au(111) has been reported[28] to produce a substantial shift of the work function (0.73 eV) that was attributed to a surface dipole. The corresponding surface potential variation produces electron scattering, and therefore, we attribute the origin of the surface-state confinement to such a dipolar interaction.

In conclusion, we have demonstrated that molecular self-assembly provides an intrinsically parallel method to impose novel electronic properties on entire surfaces. In our study, the simple Ag(111) surface is tessellated with a chiral kagomé topology of NC−$Ph_6$−CN molecules representing a dichotomous network with two symmetrically different types of chiral pores. The purely organic adlayer confines the surface-state electrons and thus represents a supramolecularly engineered nanoarchitecture of complex quantum corrals creating a rich electronic structure in the cavities. The nontrivial geometry of the system prevents from an analytic theoretical description and rather calls for a numeric approach. The presented BEM simulations allow a thorough analysis of the electron scattering properties evidenced by the detailed reproduction of the experimental findings. We expect our work to open new avenues toward large-scale

nanopatterning of complex electronic states and their understanding through reliable model calculations.

**Acknowledgment.** This work has been supported by the European Science Foundation Collaborative Research Programme FunSMARTs, the TUM Institute of Advanced Studies, the DFG Cluster of Excellence Munich Center for Advanced Photonics, the Spanish MICINN (MAT2007-66050), the EU (NMP4-SL-2008-213660-ENSEMBLE), the Basque Departamento de Educación, UPV/EHU (Grant No. IT-366-07), and the Spanish Ministerio de Ciencia e Innovación (Grant No. FIS2007-6671-C02-01).

## References

(1) Crommie, M. F.; Lutz, C. P.; Eigler, D. M. *Science* **1993**, *262*, 218–220.
(2) Li, J. T.; Schneider, W. D.; Berndt, R.; Delley, B. *Phys. Rev. Lett.* **1998**, *80*, 2893–2896.
(3) Braun, K. F.; Rieder, K. H. *Phys. Rev. Lett.* **2002**, *88*, 096801.
(4) Manoharan, H. C.; Lutz, C. P.; Eigler, D. M. *Nature* **2000**, *403*, 512–515.
(5) Moon, C. R.; Mattos, L. S.; Foster, B. K.; Zeltzer, G.; Manoharan, H. C. *Nat. Nanotechnol.* **2009**, *4*, 167–172.
(6) Fiete, G. A.; Heller, E. J. *Rev. Mod. Phys.* **2003**, *75*, 933–948.
(7) Stepanyuk, V. S.; Niebergall, L.; Hergert, W.; Bruno, P. *Phys. Rev. Lett.* **2005**, *94*, 187201.
(8) Sentef, M.; Kampf, A. P.; Hembacher, S.; Mannhart, J. *Phys. Rev. B* **2006**, *74*, 153407.
(9) Correa, A. A.; Reboredo, F. A.; Balseiro, C. A. *Phys. Rev. B* **2005**, *71*, 035418.
(10) Silly, F.; Pivetta, M.; Ternes, M.; Patthey, F.; Pelz, J. P.; Schneider, W. D. *Phys. Rev. Lett.* **2004**, *92*, 016101.
(11) Oncel, N.; van Houselt, A.; Huijben, J.; Hallback, A. S.; Gurlu, O.; Zandvliet, H. J. W.; Poelsema, B. *Phys. Rev. Lett.* **2005**, *95*, 116801.
(12) Pennec, Y.; Auwärter, W.; Schiffrin, A.; Weber-Bargioni, A.; Riemann, A.; Barth, J. V. *Nat. Nanotechnol.* **2007**, *2*, 99–103.
(13) Didiot, C.; Pons, S.; Kierren, B.; Fagot-Revurat, Y.; Malterre, D. *Nat. Nanotechnol.* **2007**, *2*, 617–621.
(14) Stepanyuk, V. S.; Negulyaev, N. N.; Niebergall, L.; Longo, R. C.; Bruno, P. *Phys. Rev. Lett.* **2006**, *97*, 186403.
(15) Schiffrin, A.; Reichert, J.; Auwarter, W.; Jahnz, G.; Pennec, Y.; Weber-Bargioni, A.; Stepanyuk, V. S.; Niebergall, L.; Bruno, P.; Barth, J. V. *Phys. Rev. B* **2008**, *78*, 035424.
(16) Barth, J. V. *Annu. Rev. Phys. Chem.* **2007**, *58*, 375–407.
(17) Schlickum, U.; Decker, R.; Klappenberger, F.; Zoppellaro, G.; Klyatskaya, S.; Auwärter, W.; Neppl, S.; Kern, K.; Brune, H.; Ruben, M.; Barth, J. V. *J. Am. Chem. Soc.* **2008**, *130*, 11776–11782.
(18) Kühne, D.; Klappenberger, F.; Decker, R.; Schlickum, U.; Brune, H.; Klyatskaya, S.; Ruben, M.; Barth, J. V. *J. Am. Chem. Soc.* **2009**, *131*, 3881–3883.
(19) Clair, S. *Ph.D. thesis*, Ecole Polytechnique Federale de Lausanne, 2004.
(20) Tersoff, J.; Hamann, D. R. *Phys. Rev. B* **1985**, *31*, 805–813.
(21) Lang, N. D. *Phys. Rev. B* **1986**, *34*, 5947–5950.
(22) Li, J. T.; Schneider, W. D.; Berndt, R. *Phys. Rev. B* **1997**, *56*, 7656–7659.
(23) Jeandupeux, O.; Bürgi, L.; Hirstein, A.; Brune, H.; Kern, K. *Phys. Rev. B* **1999**, *59*, 15926–15934.
(24) Myroshnychenko, V.; Carb-Argibay, E.; Pastoriza-Santos, I.; Perez-Juste, J.; Liz-Marzan, L. M.; Garcia de Abajo, F. J. *Adv. Mater.* **2008**, *20*, 4288–4293.
(25) Bürgi, L.; Jeandupeux, O.; Hirstein, A.; Brune, H.; Kern, K. *Phys. Rev. Lett.* **1998**, *81*, 5370–5373.
(26) Gross, L.; Moresco, F.; Savio, L.; Gourdon, A.; Joachim, C.; Rieder, K. H. *Phys. Rev. Lett.* **2004**, *93*, 056103.
(27) *HYPERCHEM 7.5*; Hypercube, Inc.: 1115 NW 4th St., Gainesville, FL.
(28) France, C. B.; Parkinson, B. A. *Appl. Phys. Lett.* **2003**, *82*, 1194–1196.

NL901700B